Hall2De Simulations of a 12.5-kW Magnetically Shielded Hall Thruster for the NASA Solar Electric Propulsion Technology Demonstration Mission

IEPC-2015-254／ISTS-2015-b-254

Presented at the Joint Conference of 30th International Symposium on Space Technology and Science
34th International Electric Propulsion Conference and 6th Nano-satellite Symposium,
Hyogo-Kobe, Japan
July 4 – 10, 2015

Ioannis G. Mikellides,* Alejandro Lopez Ortega,† Richard R. Hofer‡ and James E. Polk,§
Jet Propulsion Laboratory, California Institute of Technology, Pasadena, CA, 91109, USA

Hani Kamhawi** and John T. Yim††
NASA Glenn Research Center, Cleveland, Ohio, 44135, USA

James Myers‡‡
Vantage Partners LLC, 3000 Aerospace Pkwy, Brook Park, Ohio 44142, USA

The Hall Effect Rocket with Magnetic Shielding (HERMeS) is a 12.5-kW Hall thruster under development by the NASA Glenn Research Center and the Jet Propulsion Laboratory for the Space Technology Mission Directorate's Solar Electric Propulsion Technology Demonstration Mission. Its performance and throughput capability are expected to meet or exceed the requirement for the proposed Asteroid Redirect Mission concept, the first robotic mission under development by NASA to visit a large near-Earth asteroid, collect a multi-ton boulder from its surface and redirect it into a stable orbit around the moon. Numerical simulations performed with Hall2De have guided the design of the magnetic shielding topology in HERMeS. The results at the highest discharge current (31.3 A) and highest discharge voltage (800 V) operating conditions yield ion energies at the outer and inner discharge channel walls that are in most cases below the estimated ion energy sputtering threshold for the boron nitride walls. In locations where this is not the case the erosion rate is found to be ≤ 2×10^{-12} mm/h. Also, wall probe measurements of the plasma potential and electron temperature yield near-anode values and ≤ 5eV respectively along the channel surfaces, and are in agreement with the simulation results at these two operating conditions. These results demonstrate that magnetic shielding of the HERMeS channel has been achieved. Simulation results for the incident power to the thruster walls from the plasma are also presented. Observed trends in the thermal response of the thruster during recent testing with varying applied magnetic field (at constant power) are reproduced by the simulations. The trends are discussed in the context of the plasma evolution at the highest power, highest discharge voltage operating condition of 12.5 kW and 800 V.

* Principal Engineer, Electric Propulsion Group, Ioannis.G.Mikellides@jpl.nasa.gov
† Member of the Technical Staff, Electric Propulsion Group, Alejandro.Lopez.Ortega@jpl.nasa.gov
‡ Senior Engineer, Electric Propulsion Group, richard.r.hofer@jpl.nasa.gov
§ Principal Engineer, Propulsion, Thermal, and Materials Systems Group, James.E.Polk@jpl.nasa.gov
**** Research Engineer, Electric Propulsion Branch, hani.kamhawi-1@nasa.gov
†† Research Engineer, Electric Propulsion Branch, john.t.yim@nasa.gov
‡‡ Senior Aerospace Engineer, james.l.myers@nasa.gov

I. Introduction

NASA is developing the first robotic mission to visit a large near-Earth asteroid, collect a multi-ton boulder from its surface (Fig 1-left), and redirect it into a stable orbit around the moon. Once there, astronauts will explore it and return to Earth with samples in the 2020s. This proposed Asteroid Redirect Mission (ARM) concept is part of NASA's plan to advance the new technologies and spaceflight experience needed for a human mission to the Martian system in the 2030s. The performance and throughput capability of high-power (20-100 kW) Hall thrusters impacts a wide range of government and commercial space applications including payload delivery, orbital debris removal, deep space human exploration and science missions, and is now the leading Solar Electric Propulsion (SEP) technology for ARM. For example ARM optimizes by using SEP with I_{sp}=3000 s and 10,000 kg of xenon throughput capability (for a 40 kW power system) [1, 2]. Until recently, 10,000 kg of xenon would constitute a significant extension over the demonstrated capabilities of SEP. For example, this value is nearly a factor 25 greater than the 425 kg launched on the Dawn mission, the largest xenon propellant load launched to date. However, after recent breakthrough advances enabled by magnetic shielding [3, 4], Hall thrusters are now expected to meet or exceed such throughput requirements. In response to the wide-ranging impact of high-power Hall thrusters, NASA's Space Technology Mission Directorate (STMD), through its SEP Technology Demonstration Mission (TDM) program is funding the development of the **H**all **E**ffect **R**ocket with **M**agn**e**tic **S**hielding (**HERMeS**), a 12.5-kW class level, Hall thruster (Fig 1-right). The main objective of the SEP TDM is to demonstrate the performance and high-throughput capability of a high-power Hall thruster in space during a demonstration mission planned for later in this decade. The development of HERMeS is a joint effort between the NASA Glenn Research Center (GRC) and the Jet Propulsion Laboratory (JPL) and incorporates extensive experience in the design, modeling and testing of Hall thrusters. Additional information about the ongoing HERMeS development activities is provided in our companion papers [5-8].

Of critical importance in the development of HERMeS have been the recent advances associated with magnetic shielding. The technique has been demonstrated to eliminate channel erosion in Hall thrusters [4, 9, 10] based on findings from physics-based numerical simulations with a magnetic-field-aligned-mesh (MFAM) code called Hall2De [11] and results from a Qualification Life Test of Aerojet-Rocketdyne's XR-5 (formerly known as BPT-4000) [3]. Magnetic shielding enforces the equipotentialization of specific magnetic field lines called "grazing lines" which, in turn, protect the channel walls from ion bombardment. The demonstration of the first principles of magnetic shielding took place at JPL in 2010-2012 when a 6-kW laboratory Hall thruster called H6 [12], was modified from its original configuration (called H6US) based on the guidance of numerical simulations with Hall2De. The magnetically shielded configuration, or H6MS, was then wear tested for 150 h at 300 V, 6 kW (20 A) and the erosion rates of the acceleration channel were found to be 2-3 orders of magnitude lower than those in the H6US [10]. These measured rates were in agreement with the numerical simulation predictions [9]. A similar effort ensued with the NASA 300M, a 20-kW Hall thruster developed at GRC [13]. The thruster was modified from its original configuration based on the guidance of numerical simulations [14] and then tested to demonstrate that magnetic shielding could be achieved at discharge powers greater than 6 kW. Discharge channel deposition of back-sputtered products from the vacuum facility, and plasma potential and electron temperature measurements obtained on the inner and outer channel surfaces confirmed that magnetic shielding was achieved [15]. More recently, numerical simulations of the H6MS were performed for the discharge voltage range of 400-700 V at constant power (6 kW) and at 800 V, 9 kW [16]. The simulations were followed by performance and wear testing at the 800-V, 9-kW operating condition [17]. The combination of simulations and short tests showed that the effectiveness of magnetic shielding to reduce channel erosion by at least a few orders of magnitude was retained at higher discharge voltages so long as the magnetic circuit was capable of supplying the intended magnetic field topology [18]. The experience gained in the development of magnetically shielded Hall thrusters over the last several years was applied to HERMeS using a variety of thermal, structural and plasma models that helped guide the design. In this article we discuss parts of the effort associated with the plasma modeling.

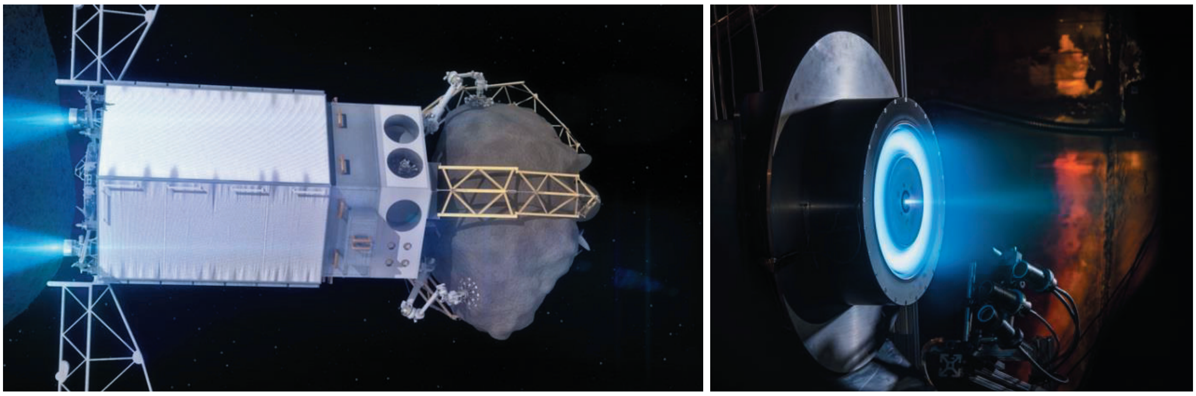

Fig 1. Left: The proposed ARM concept is the first robotic mission to visit a large near-Earth asteroid, collect a multi-ton boulder from its surface, and redirect it into a stable orbit around the moon. ARM is part of NASA's plan to advance the new technologies needed for a human mission to Mars, and will require long-life Hall thrusters that can deliver 3000 s of I_{sp} (input voltage to each thruster of ~800 V). Right: HERMeS is a 12.5-kW class thrusters being developed by NASA GRC and JPL for the STMD SEP TDM Program to demonstrate in space the SEP capabilities needed for ARM and beyond.

The main objectives of the plasma modeling and simulation work have been, first, to provide guidance to the design of the magnetic shielding topology in HERMeS and to verify its effectiveness to protect the channel walls from erosion. Second, to support life qualification activities by providing predictions of plasma fluxes to the various surfaces, for the purpose of assessing potentially life-limiting mechanisms associated with sputtering and/or thruster heating. Section IIIA describes results of numerical simulations aimed at assessing the effectiveness of magnetic shielding in HERMeS. In addition to providing predicted erosion rates at the channel walls, we also compare results of predicted plasma properties along the walls with recent wall probe measurements. Results for the computed incident power to the channel walls by electron and ions are discussed in Sec. IIIB. These plasma loads are used in a detailed 3-D thermal model of HERMeS to predict the thermal response of the thruster. The thermal model details and related results are reported in one of our companion papers [8].

II. Computational Methods

A. General description and recent advancements of Hall2De

The numerical simulations presented in this paper have been performed with the Hall2De code, a two-dimensional (2-D), axisymmetric computational solver of the conservation equations that govern the evolution of the partially ionized gas in Hall thrusters [11, 19]. The governing equations, numerical methodology, various thruster simulations and comparisons with measurements have been presented elsewhere [11, 20, 21]. Here, we provide only a brief overview for completeness and outline physics and algorithm advancements implemented recently in the code.

In Hall2De all governing equations are solved on a magnetic-field-aligned computational mesh (MFAM). The solution of the electron energy conservation equation is obtained semi-implicitly; the thermal conduction and current convection terms are implicit whereas all other terms are evaluated explicitly. Current conservation, incorporating Ohm's law to solve for the electron current density, is also solved implicitly. Ohm's law is solved in the frame of reference of the magnetic field with the electrical resistivity accounting for contributions from collisions of electrons with all other species. It is now widely accepted that transport of electrons in Hall thrusters is driven to a large extent by non-classical mechanisms, possibly by plasma turbulence [22-27]. In numerical simulations this non-classical transport has typically been modeled using an effective or "anomalous" collision frequency. Denoting this collision frequency as ν_α, we impose in Hall2De a so-called transport coefficient function $f_\alpha(r,z)$ and set $\nu_\alpha = f_\alpha \omega_{ce}$ with ω_{ce} denoting the electron cyclotron frequency. Our specification of f_α is guided by plasma measurements whenever they exist.

The numerical solution of the conservation equations for the heavy species is obtained without invoking discrete-particle methods. The evolution of the (collision-less) neutral species is computed using line-of-sight formulations that account for their depletion through ionization [19]. Ions are treated as an isothermal, cold (relative to the electrons) fluid, accounting for the drag force and the ion-pressure gradient. In 2013-2014 the algorithm for the ion hydrodynamics was completely re-written in Hall2De. The previously explicit, non-conservative, vertex-centered scheme was replaced with a semi-implicit, conservative, cell-centered scheme that allows for better accuracy and reduced computation times. Inter-cell fluxes are determined using a variant of the Harten-Lax-van Leer (HLL) scheme [28] and is better described in [29]. The equations of motion for ions are discretized in time using a semi-implicit predictor/multi-corrector [30] scheme that has shown to reduce Hall2De computation times by 3-4 times. Though relaxation times for ions can be shown to be small enough inside the acceleration channel, such times can become exceedingly high in the near plume region. If modeled as a single fluid, convection of slow ions in the near plume will occur at the mean velocity, which is dominated by the momentum of the fast ions. This would in turn result in erroneously low particle densities in regions that reside outside the main beam. To circumvent this limitation Hall2De employs a multi-fluid algorithm described in more detail in [29]. Briefly, determination of the fluid to which a given ion belongs is made upon examining the plasma potential at the location where the ion mass element was generated. So-called "threshold" potentials are specified in Hall2De to determine the maximum energy at which each ion population is created. Ions of different populations are created by ionization and charge-exchange collisions depending on how the threshold energy compares to the local value of the plasma potential. As part of testing the fidelity of the multi-fluid algorithm, Katz and Lopez Ortega also developed and implemented a PIC algorithm for ions in Hall2De. Numerical tests showed that a 2-fluid hydrodynamic solution was very close to the PIC solution in the near-plume. It was also shown that the addition of a third ion fluid did not alter the results significantly [29]. Therefore our simulations (including those presented in this paper) typically allow for two distinct ion fluids. Up to triply charged ions are also accounted for each of the two fluids yielding a total of six ion momentum and six ion continuity equations.

In the majority of the computational domain the assumption of quasi-neutrality in the plasma is valid. Therefore, near most solid surfaces of the thruster, boundary conditions that account for the sheath may be implemented based on a thin-sheath approximation [11]. However, there are some regions near walls where the sheath can become large compared to the local computational cell size. These regions develop typically at the exit of the acceleration channel, in the vicinity of the wall edges where the turning flow undergoes significant expansion. This, in turn, can lead to very low local densities and large Debye lengths. This is exacerbated in magnetically shielded thrusters where the plasma potential gradients at the corners of the chamfered walls can become exceedingly large (if computed assuming fluid expansion of a quasi-neutral plasma) due to the highly concentrated magnetic field lines there. It is therefore also possible that the effects of the sheath modify the structure of the potential in this region and, in turn, the ion divergence angle as postulated in previous work [31, 32]. This could have important implications on erosion of the poles. In response, a new space charge algorithm has been developed in Hall2De. Briefly, at each time-step, the solution to the fluid plasma and collision-less neutrals is interrogated to identify regions near the thruster walls where the local Debye length is larger than the distance from the cell centroid to the nearest wall. When this is the case, Poisson's equation is solved to determine the space charge potential. This new potential (instead of that determined by Ohm's law) is then employed to compute the electric field, which is used in the next time step to determine the ion momentum. The details of the algorithm and simulations results are provided in our companion paper [33]. The simulations have shown that although the potential structure at these small regions near the chamfered corners of the channel can indeed be modified compared to the previous (hydrodynamic, quasi-neutral) solution, the effectiveness of the magnetic shielding remains intact. This is because the Debye length decreases rapidly upstream of these corners, so that the near-anode potential values remain largely unchanged along the chamfered walls. Therefore, since one of the main topics of this paper is the assessment of the effectiveness of magnetic shielding to protect the channel walls in HERMeS, all simulations presented herein do not incorporate the new space charge algorithm in Hall2De.

B. **Computational arrangement and simulation conditions for HERMeS**

Typically in Hall2De the MFAM spans a computational domain in r-z geometry that extends several times the thruster channel length in the axial direction, and encompasses the cathode boundary and the thruster centerline. In the present simulations the near-plume computational domain spanned approximately 8.75 and 12.5 times the acceleration channel length L in the radial and axial directions, respectively. Shown in Fig 2 is a schematic of the computational domain for the HERMeS simulations with naming conventions of various thruster components and boundaries.

The conservation equations solved by Hall2De are closed with boundary conditions (BC) at all surfaces. Referring to Fig 2, we impose dielectric BCs at the outer and inner channel insulators of the acceleration channel in HERMeS. For all dielectric-wall boundaries a zero-current condition is imposed. At these surfaces the BC for the convective heat loss follows the formulations of Hobbs and Wesson [34] for the potential drop in a sheath with secondary electron emission and is further discussed in Sec. IIIB. In HERMeS the poles are coated with a thin layer of alumina. These poles have therefore been modeled also as dielectric boundaries. At the anode we impose (conducting) sheath BCs for the electron current density normal to the anode, and are also further discussed in Sec. IIIB. Propellant injection is modeled as influx BCs and specified at two edge edges emulating the thruster ports adjacent to the outer and inner channel walls, as shown in Fig 2-left. At the cathode boundary the neutral particle flux, ion flux, plasma potential and electron temperature are specified. The far plume solution is subject to outflow BCs along which a zero-current condition and a fixed electrons temperature are imposed. Though HERMeS has been tested under several operation conditions, ranging 300-800 V, 4.7-12.5 kW (15.6-31.3 A) [7], we present here results for only two operating conditions: (1) 9.4 kW, 300 V (31.3 A) and (2) 12.5 kW, 800 V (15.6 A). These constitute conditions of maximum discharge current and maximum discharge voltage, respectively. The simulation specifications for these conditions are provided in Table 1. For brevity we will be referring to these two operating conditions as the 9.4-kW and 12.5-kW conditions. Also, throughout this paper cases that involve different values of the maximum radial component of the applied magnetic field will be normalized to the nominal value of the 12.5-kW condition.

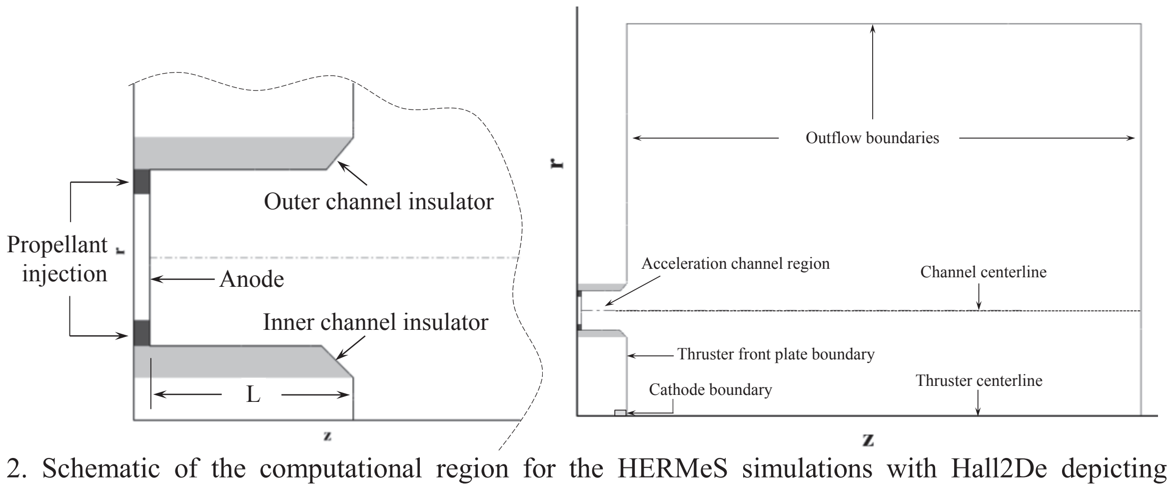

Fig 2. Schematic of the computational region for the HERMeS simulations with Hall2De depicting relevant naming conventions used throughout this article.

Table 1. The HERMeS simulations with Hall2De have been performed at the maximum discharge current and maximum discharge voltage conditions. The latter is also the maximum power condition.

	Max Discharge Current Condition	Max Discharge Voltage Condition
Discharge power (kW)	9.4	12.5
Discharge voltage (V)	300	800
Discharge current (A)	31.33	15.63
Anode flow rate (kg/s)	2.72×10^{-5}	1.73×10^{-5}
Cathode flow rate (kg/s)	0.19×10^{-5}	0.19×10^{-5}
Normalized magnetic field*	1.154	1

*Refers to the normalized value of the maximum radial component, $B_{r,max}$, at the channel centerline under nominal operating conditions.

III. Numerical Simulations

The simulations presented in this section have been motivated by two main objectives, both associated directly with the life of the thruster. The first is to assess the effectiveness of the magnetic shielding design in HERMeS to protect the channel walls from erosion. The sensitivity of the magnetic shielding to uncertainties in the precise location of the plasma relative to the anode is also quantified. The thermal design of HERMeS is guided by a detailed 3-D thermal model of the thruster that depends upon knowledge of the power deposition by the plasma to its various surfaces. So the second objective of the work in this paper is to determine the plasma loads from Hall2De and explain critical trends in both the simulations and recent temperature measurements that could affect the integrity of the thermal design. The details of and results from the 3-D thermal model of HERMeS, which is developed at NASA GRC, are provided in a companion paper [8]. Here we present only the results from the Hall2De simulations and discuss trends associated with variations in the magnitude of the applied magnetic field, which is of significance to specifying margins associated with the operation and life of HERMeS. All simulations have been performed using two (fast and slow) ion fluid populations. Three charge states have been accounted for each of the two ion populations.

A. **The effectiveness of magnetic shielding in HERMeS**

Prior to the fabrication of HERMeS, the design of the thruster incorporated lessons learned from previous experience with high-power Hall thrusters at NASA but also relied heavily on models to guide specific areas of the design. Most prominent were the magnetic, thermal and plasma modeling efforts. The design of the magnetic field was performed by a combination of magnetic and plasma modeling. The specific topology of the field was based largely on the magnetic shielding first principles outlined in several previous publications on the subject [3, 4, 9]. In this section we present results from Hall2De numerical simulations of HERMeS aimed at demonstrating the effectiveness of the magnetic shielding design, and compare with recent wall probe measurements of plasma properties along the channel.

The first principles of magnetic shielding were described in detail in several other publications so we only provide here a summary of the basic concepts for completeness. Referring to Fig 3-right, magnetic shielding is achieved by way of a magnetic field topology that sustains high plasma potentials and low electron temperatures along the channel-grazing magnetic field lines. In this manner the incident-ion kinetic and sheath energies can be marginalized. Moreover, with a properly designed combination of the magnetic field topology and channel geometry, the electric field can be controlled to be both nearly perpendicular to the surface and large in magnitude, as shown in the magnetically shielded configuration in Fig 3-right. In this manner the perpendicular component of the electric field forces ion acceleration away from walls without loss of thruster performance, which also reduces the wall-incident ion flux. The key principle behind magnetic shielding lies in the recognition that the electron pressure forces the electric and magnetic fields to no longer form an orthogonal set (Fig 3-left). Thus, a geometry of magnetic field lines simply with convex curvature toward the anode cannot effectively control the electric field near surfaces (and, in turn, the erosion) if the near-wall lines are not also equipotential. In contrast, Fig 3-right shows a magnetically shielding topology. This topology eliminates the contribution of the electron pressure by exploiting those magnetic field lines that extend deep inside the acceleration channel, near the anode. Because these lines are associated with high potential and low electron temperature values the contribution of the electron pressure is marginalized.

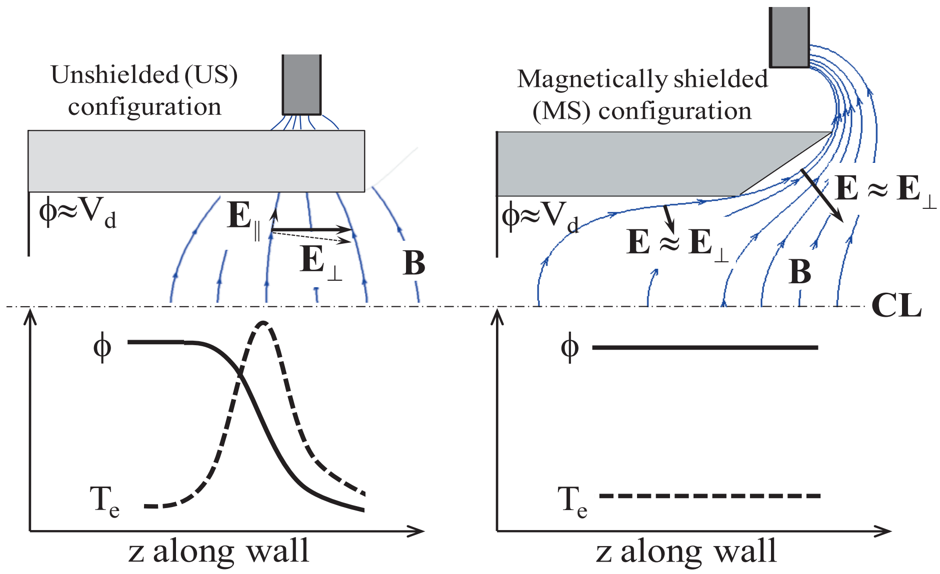

Fig 3. Schematics of the upper half of the annular acceleration channel in a typical magnetic-layer Hall thruster (top) and typical profiles of the plasma potential and electron temperature (bottom) along the channel wall. Left: Representative magnetic field lines and profiles along the wall in an unshielded configuration. Right: Representative magnetic field lines and profiles along the wall in a magnetically shielded configuration. The line that extends deepest into acceleration channel and runs closest to the channel wall without crossing it is termed the "grazing line."

Two series of sensitivity analyses have been performed in the magnetic shielding simulations, both motivated by the need to quantify uncertainties and impose margins. The first series is related to our uncertainty in the precise location of the acceleration zone relative to the channel exit. As mentioned in Sec. IIA, it is well known that numerical simulations like those performed with Hall2De and other Hall thruster codes [35, 36], are challenged by our limited understanding of the anomalous electron transport coefficients. As a result, in most cases, simulations rely on experimental measurements to guide the variation of the anomalous collision frequency in the discharge. Both past work with smaller Hall thrusters [37, 38] and more recent work with the H6MS [21] have proposed that probes injected into the discharge – a commonly-used diagnostic for measuring the plasma properties in these devices - perturb the plasma. In even more recent experiments with the H6MS, Laser Induced Fluoresce measurements (a non-intrusive diagnostic) have revealed that one of the main effects of the perturbation is the displacement of the acceleration zone by several mm.[§§] Therefore, in both the experiments and the numerical simulations (which in part rely on the measurements) there remains an uncertainty of $z/L<0.25$ on the precise location of the plasma.

[§§] These measurements are planned for publication in the near future.

In this section we investigate the sensitivity of magnetic shielding on the location of the plasma in the simulations, at the 9.4-kW condition. The displacement of the plasma was achieved by retaining the same profile of the anomalous collision frequency but simply displacing it axially by some specified amount. The magnitude of the frequency was also changed (by iteration) in each simulation until the discharge current at which the thruster was operated was achieved. In the simulations presented here we have displaced the plasma by z/L~0.3 as shown in Fig 4-left. The three different locations z/L identified in Fig 4-left refer to the location of the maximum computed electron temperature at the channel centerline. The maximum value of the radial component of the magnetic field, $B_{r,max}$, along the channel centerline was held fixed at $B_{r,max}$=1.154 in all these simulations.

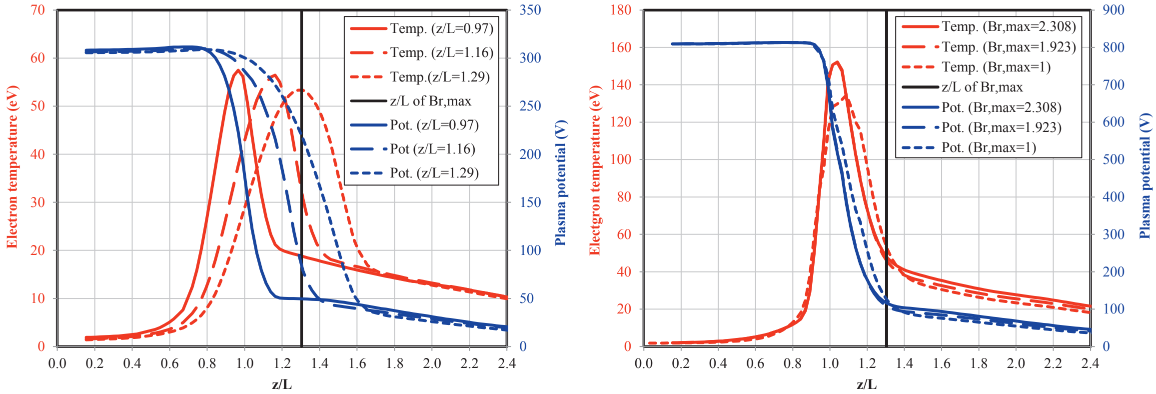

Fig 4. Computed plasma potential and electron temperature along the channel centerline. Left: Profiles at the 9.4-kW operating condition for three z/L locations of the acceleration zone. The different values of z/L in the legend designate the location of the maximum electron temperature. The maximum value of the radial component of the magnetic field along the channel centerline, $B_{r,max}$=1.154 for all cases. Right: Profiles at the 12.5-kW operating condition for three values of $B_{r,max}$.

Simulation results at the 9.4-kW condition for the three different locations of the plasma are shown in Fig 5. The 2-D contours display plasma potential (top) and electron temperature (bottom). Also overlaid on these plots are values of these variables at several representative locations. It is seen that the plasma potential along the chamfered regions of the channel walls remains at near-anode-potential values. Also, the electron temperature in these regions remains at low values, not exceeding a few eV. These values are attained for all three cases showing the insensitivity of magnetic shielding to uncertainties associated with the anomalous collision frequency and related locations of the acceleration zone. This does not mean of course that such uncertainties are not important since the precise location of the acceleration zone could have significant implications for example on pole erosion. Therefore a separate effort is ongoing to derive the dominant physics of the anomalous transport and implement a self-consistent model in Hall2De. Preliminary results of this effort are presented in our companion paper [39].

Though recent testing of HERMeS has shown that optimal operation of the thruster occurs at magnetic field strengths lower than the value at which saturation of the magnetic circuit components occurs [7], it is important to identify the circuit's margins. We therefore performed a series of Hall2De simulations in which the magnitude of the magnetic field was varied. The location of the acceleration zone was not varied in these simulations; it was chosen based on previous simulations with the H6MS [18]. The variation of the plasma potential and electron temperature along the channel centerline for the three values of $B_{r,max}$ is plotted in Fig 4-right. The range chosen for the simulations, 1-2.308, covers nominal operation as well as values close to magnetic circuit saturation.

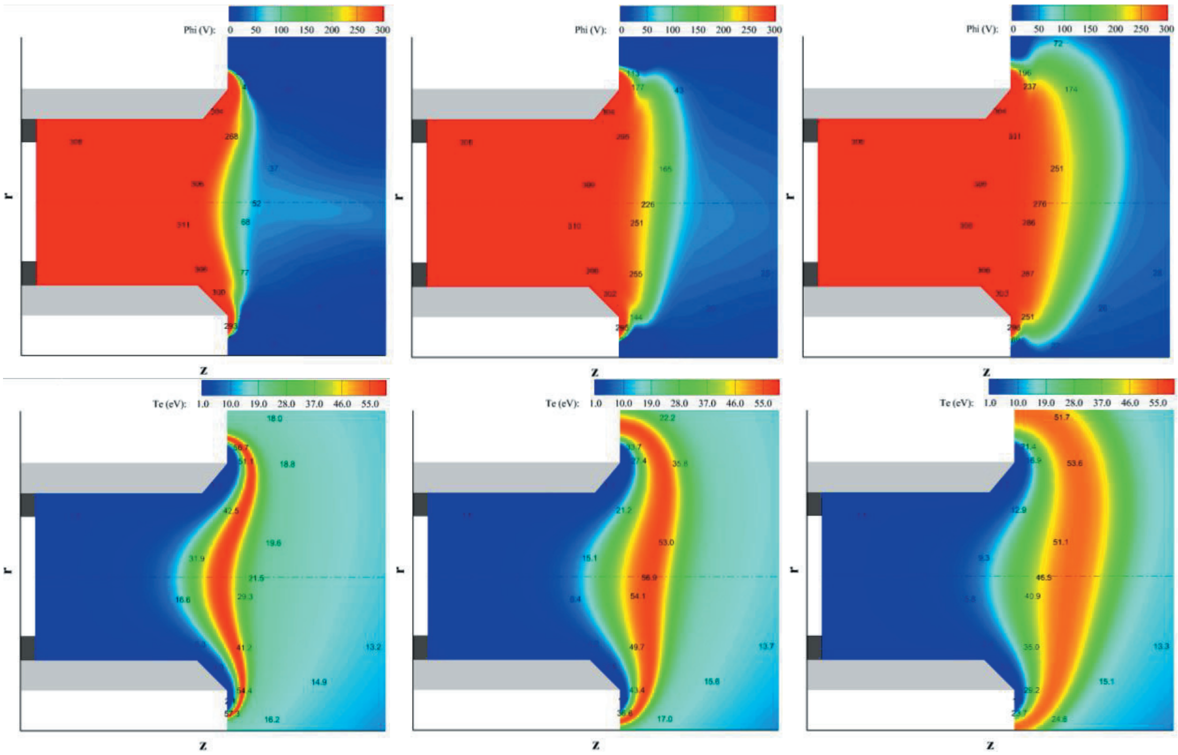

Fig 5. 2-D contours of the plasma potential (top) and electron temperature (bottom) at the 9.4-kW operating condition at three different locations of the acceleration zone: z/L=0.97, 1.16, 1.29 (from left to right). Overlaid on the contours are values of these variables at several representative locations.

Results on the sensitivity of magnetic shielding on the applied magnetic field are shown in Fig 6. Here we have chosen the 12.5-kW operating condition which is also the maximum power and maximum discharge voltage condition. By choosing this condition therefore we are also aiming at confirming the conclusions of our previous simulations results for the H6MS which showed that magnetic shielding remained effective in the range of 300-800 V [18]. We found similar insensitivity of magnetic shielding on the applied magnetic field as that found on the location of the acceleration zone in the 9.4-kW simulations. We find that for all three values of $B_{r,max}$ the plasma potential along the chamfered regions remains at near-anode-potential values and the electron temperature does not exceeding a few eV. This is not surprising since magnetic shielding is largely dependent on the topology of the field (especially the details of the grazing line), not the magnitude so long as stable operation of the discharge can be established. When the operation is stable and the topology remains unchanged then the near-anode plasma is expected to remain at near-anode potentials and low electron temperature. In turn, these values will be retained along the grazing line and therefore along the channel walls including the chamfered regions. For both the 9.4-kW and 12.5-kW conditions we find that in most cases the energy of ions striking the wall is below the assumed threshold of energy/charge (E/q) of 35 eV [9] for sputtering of the channel material. In locations where this is not the case the erosion rate is found to be extremely low, $\leq 2\times10^{-12}$ mm/h. The results for the maximum computed erosion along the channel walls are tabulated in Table 2. For the details of the sputtering yield model used in these calculations the reader is referred to Ref. [32].

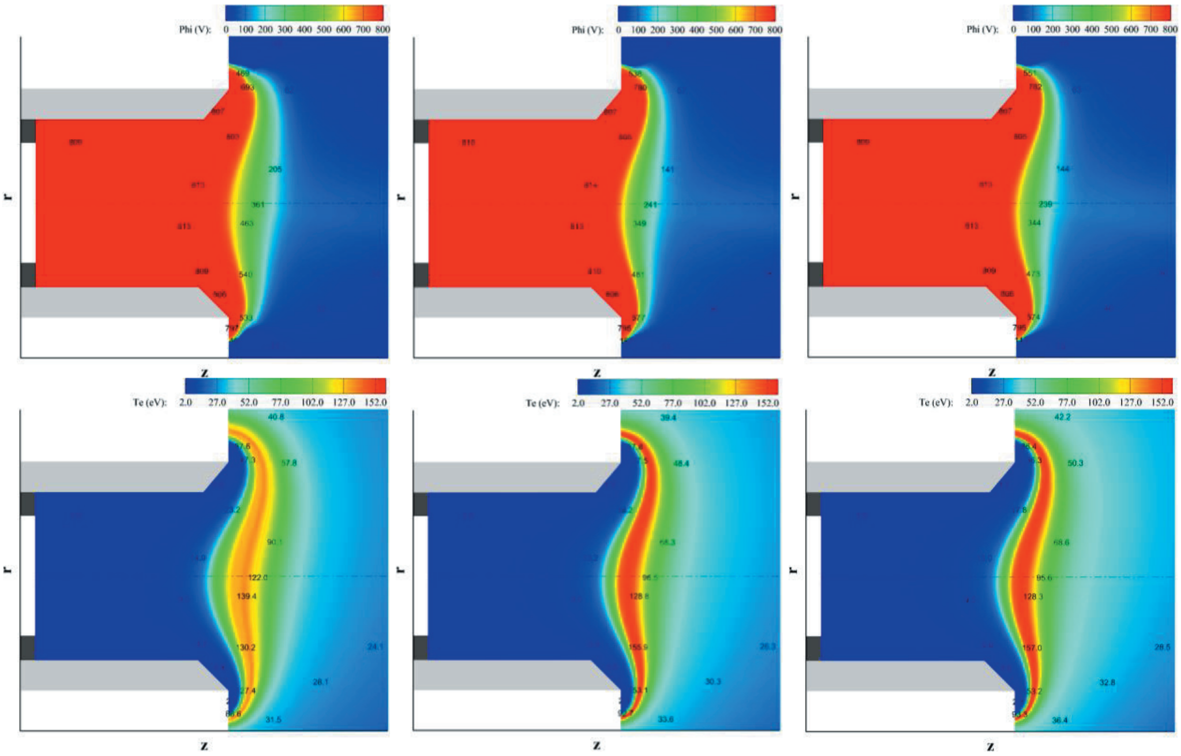

Fig 6. 2-D contours of the plasma potential (top) and electron temperature (bottom) at the 12.5-kW operating condition at three different values of the normalized applied magnetic field: $B_{r,max}$=1, 1.923, 2.308 (from left to right). Overlaid on the contours are values of these variables at several representative locations.

Table 2. Computed maximum erosion rates at the inner and outer channel walls from the HERMeS simulations at the 9.4-kW and 12.5-kW operation conditions. EBT=(ion) Energy Below (sputtering yield) Threshold. The value of the energy threshold was assumed to be E/q=35 V.

Operating Condition	Maximum Erosion Rate (mm/h)	
	Inner Wall	Outer Wall
9.4 kW, z/L=0.97	EBT	EBT
9.4 kW, z/L=1.16	EBT	7×10^{-14}
9.4 kW, z/L=1.29	EBT	EBT
12.5 kW, $B_{r,max}$=1	EBT	2×10^{-12}
12.5 kW, $B_{r,max}$=1.923	EBT	1.3×10^{-15}
12.5 kW, $B_{r,max}$=2.308	EBT	EBT

The simulation results on the effectiveness of magnetic shielding have been confirmed by recent measurements conducted at NASA GRC. In these experiments, Langmuir probes were flush-mounted in the inner and outer channel walls of the thruster. Figure 7 depicts a schematic of the probe locations along the inner channel wall. The probes were also azimuthally distributed (not shown here) to maximize the axial distance between probes along the inner and outer channel wall for a given azimuthal location. Wall probes to measure the adjacent plasma potential and electron temperature in magnetically shielded thrusters have been used successfully in the past (e.g. see [40]) and are based on the approach described in Ref. [41]. A comparison of the plasma potential and electron temperature measured by wall probes 2 and 5 with those from the numerical simulations is shown in Table 3. The values from the simulations are designated as ϕ_{pS} and T_{eS}. For the 9.4-kW condition the values in Table 3 are for the maximum electron temperature location along the channle centerline of z/L=0.97 (Fig 4-left); for 12.5-kW, this location was z/L=1.06 corresponding to the $B_{r,max}$=1 solution in Fig 4-right. The experimental uncertainties for the measured plasma potential ϕ_{pE} and electron temperature T_{eE} were ±5 V and ±1 eV, respectively. Cases for which the probes did not yield a measurement are designated as "not available" (NA). The experimental values for the plasma potential were measured with respect to facility ground. During the tests the cathode-to-ground voltage was -7.7 and -9.9 V for the 9.4 kW and 12.5 kW conditions, respectively. In the simulations, the plasma potential is with respect to cathode which was set to 0 volts. For direct comparisons we have therefore added the cathode-to-ground values to the potential measurements. The wall probe measurements confirm the effectiveness of magnetic shielding at both operating conditions, in agreement with the predictions of the numerical simulations. More information on the experimental campaign with the wall probes is provided in [7, 42]. It is worth noting here that the electron temperatures measured along the HERMeS channel are in fact noticeably lower than those measured in the H6MS, which varied 6.1-9.3 eV and 6.2-13.3 eV (±15%) along the chamfered portions of the outer and inner walls, respectively [10]. Nevertheless, erosion rates in the H6MS were still found to be 2-3 orders of magnitude lower than those measured in the unshielded version of this thruster (H6US) [9, 10]. This further strengthens our predictions that magnetic shielding in HERMeS is expected to be very effective in protecting the walls from erosion.

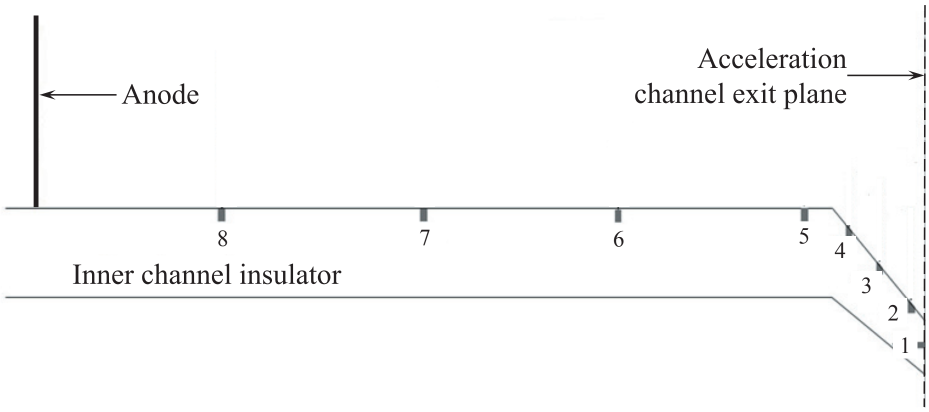

Fig 7. Location of the wall probes installed along the inner channel wall of HERMeS for the purpose of verifying magnetic shielding has been achieved. The locations of the probes along the outer wall were identical to those shown here along the inner wall.

Table 3. Comparison of the plasma potential and electron temperature, measured by wall probes 2 and 5 imbedded in the channel walls (see Fig 7), with those from the numerical simulations.

Operating Condition	Probe 2								Probe 5							
	Inner Wall				Outer Wall				Inner Wall				Outer Wall			
	ϕ_{pE}	ϕ_{pS}	T_{eE}	T_{eS}	ϕ_{pE}	ϕ_{pS}	T_{eE}	T_{eS}	ϕ_{pE}	ϕ_{pS}	T_{eE}	T_{eS}	ϕ_{pE}	ϕ_{pS}	T_{eE}	T_{eS}
9.4 kW	306	301	3	1.1	308	302	5	1.1	307	307	3	1.8	307	306	3	1.5
12.5 kW	809	805	3	1.1	808	805	4	1.1	NA	808	NA	1.8	807	808	3	1.6

B. **Power deposition by the plasma to the HERMeS discharge channel walls**

A critical aspect of the HERMeS design is its thermal response to the plasma loads during thruster operation. It is well known that when the thruster temperatures, especially those of the magnetic circuit components, are not low enough both the stability and the life of the thruster may be jeopardized. A rigorous effort has been undertaken to ensure that the thermal design of HERMeS is robust and can sustain thruster temperatures sufficiently below known limits of detrimental operation. The effort has involved extensive thermal and plasma modeling as well as measurements during thruster testing. The measurements have been provided by thermocouples installed at several critical locations on the thruster [7, 8]. An iterative process between modeling and testing has yielded several improvements in the thermal design of the thruster. Because the plasma loads to the walls is the dominant driver of the thruster temperatures we present here results of the incident power from the Hall2De simulations. Thermocouple measurements during recent testing of the thruster in a configuration that includes a radiator plate [8] have revealed that the highest temperatures in the thruster are produced during operation at the 12.5-kW condition, which is also the highest discharge power and voltage condition. Thus, though Hall2De simulations for the assessment of the thruster's thermal response have been performed at other operating conditions, we present here only results at the 12.5-kW condition. The relevant input values for the simulations are specified according to the measurements during the thruster test and are listed in Table 4.

Table 4. Operating conditions attained during the HERMeS tests at NASA GRC's Vacuum Facility-5. The same conditions have been used in the simulations with Hall2De.

Normalized magnetic field	1	1.923	2.308
Discharge current (A)	15.63	15.57	15.50
Anode flow rate (kg/s)	1.73×10^{-5}	1.57×10^{-5}	1.57×10^{-5}
Cathode flow rate (kg/s)	0.19×10^{-5}	0.11×10^{-5}	0.11×10^{-5}

The plasma power incident to the thruster surfaces is determined self-consistently by Hall2De through the specification of appropriate boundary conditions. The two sources of power deposition accounted for are ions that are accelerated through the sheath, and plasma electrons (both primary and secondary in the case of electrical insulators). Metastable atoms and photons are assumed negligible. The total power P incident to the walls is therefore the sum of the ion and electron contributions, Pi and Pe:

$$P = Pi + Pe. \tag{1}$$

The computational mesh divides each boundary into several increments or "edges" identified by iE. Thus the total power to the walls is the sum of all the increments of power deposited to each edge, ΔPi_{iE} and ΔPe_{iE}

$$Pi = \sum_{iE} \Delta Pi_{iE} \qquad Pe = \sum_{iE} \Delta Pe_{iE}\,. \tag{2}$$

Eliminating the subscript iE from Eq. (2) for simplicity, the incident power increment associated with ions may be expressed as

$$\Delta Pi = \sum_{iZ}\sum_{iF} q_{iZ}\boldsymbol{\Gamma}_{iZ,iF} \cdot \Delta\mathbf{A}\left(\tfrac{1}{2}T_e + \phi_S + K_{iZ,iF} + \varepsilon_{iZ}\right) \tag{3}$$

where $\boldsymbol{\Gamma}_{iZ,iF}$ in Eq. (3) is the ion flux at the pre-sheath edge for ion fluid population iF and charge state iZ, and ΔA is the surface area associated with edge iE. The ion charge at state iZ is given by q_{iZ}. The potential energy flux at each surface associated with the acceleration of ions through the sheath of magnitude ϕ_S is proportional to $\boldsymbol{\Gamma}\cdot\hat{\mathbf{n}}\,(\tfrac{1}{2}T_e+\phi_s)$ where $\hat{\mathbf{n}}$ is the unit norm to the edge. The $\tfrac{1}{2}T_e$ appears because the ions are assumed to enter the sheath with the Bohm velocity in order to satisfy the Bohm criterion. For ions to acquire this velocity the pre-sheath imposes a potential at the sheath edge that equals $\tfrac{1}{2}T_e$. The sheath magnitude is determined depending on whether the boundary is an electrical conductor or insulator:

$$\phi_s = \begin{cases} \phi_p - V & \text{conductor} \\ \phi(Y_e) & \text{insulator} \end{cases} \tag{4}$$

For a conductor, ϕ_p in Eq. (4) is the plasma potential computed at the center of the computational cell adjacent to the boundary edge and V is the voltage applied to that boundary. In the case of an insulator, the sheath depends on the secondary electron yield Y_e and is computed based on the formulations Hobbs and Wesson [34]. Both the implementation of the formulation in Hall2De and the dependence of Y_e on the electron temperature have been provided in previous articles [3, 11]. The kinetic energy flux for each ion of charge and fluid states iZ and iF respectively is given by $K_{iZ,iF}=½mu_{iZ,iF}^2/iZ$ where $\mathbf{u}_{iZ,iF}$ is the ion velocity at the pre-sheath edge and m is the ion mass. As mentioned previously, in the HERMeS simulations the maximum number of iF is 2. The last term in the parenthesis of Eq. (3) accounts for the power released at the surface by recombination of ions with ε_{iZ} being the ionization potential of the ion with charge state iZ.

For electrons, the power deposited at each boundary edge is given by

$$\Delta Pe = j_{Te} \Delta A \exp\left(-\bar{\phi}_s\right) f T_e \tag{5}$$

where the thermal current density is given in Eq. (5) by $j_{Te}=q_e n_e (q_e T_e/2\pi m_e)^{½}$ and $\bar{\phi}_s=\phi_s/T_e$. By assuming that the absorbed electrons are characterized by a Maxwellian distribution function it has been shown that the average energy of electrons leaving the plasma is $(2T_e+\phi_s)$ as shown in Eq. (6) [43]. In the case of an insulator the secondary electron emission must be taken into account leading to the following expressions for *f* in the two types of electrical boundary conditions:

$$f = \begin{cases} 2+\bar{\phi}_s & \text{conductor} \\ \dfrac{2+(1\text{-}Y_e)\bar{\phi}_s}{1+\dfrac{Y_e}{2}\dfrac{\exp\left(-\bar{\phi}_s\right)}{\sqrt{\pi\bar{\phi}_s}}} & \text{insulator} \end{cases} \tag{6}$$

1) Results

The results from thermocouple measurements during recent HERMeS testing are plotted in Fig 8 for the outer (left) and inner (right) channel walls. Three measurements are provided along the outer channel and three along the inner channel. The three thermocouples along each wall were placed at different locations to capture any axial variations of the temperature along the channel. The precise locations are of no major significance in this investigation and are only used loosely to establish qualitative trends and comparisons with the simulations. We term these locations as downstream (DS), middle (MD) and upstream (US) to identify their approximate position in the channel. Referring to Fig 2-left, the DS thermocouple is nearest to the exit plane whereas the US thermocouple is nearest to the anode. The MD location is approximately in the middle of the channel.

The following trends can be observed from these measurements. (1) The MD location is hotter than the other two locations for all magnetic field strengths. Also, in all cases except one, the US location is the coolest; the one case the latter does not occur is at $B_{r,max}$=1 between the DS and US locations along the inner wall but these values are within 4 ^{o}C of each other (see Fig 8-right). (2) At each location, the coolest temperatures are achieved at the lowest magnetic field value of $B_{r,max}$=1; at the outer wall the hottest temperatures occur at $B_{r,max}$=1.923 whereas at the inner wall they occur at $B_{r,max}$=2.308, though all values between the two high field cases at each location are within 20 ^{o}C of each other. (3) At a given location on the channel, the outer wall is consistently hotter than the inner wall.

Also plotted in Fig 9 are results from Hall2De simulations for the incident power to the walls from the plasma based on the energy flux BCs described above. The results show similar trends with the experiment. Specifically, we found that the lowest power deposition occurs at the lowest magnetic field and that the incident power is lower to the inner channel than it is to the outer channel. Also, for the simulation conditions outlined in Table 4, we found that the incident power at $B_{r,max}$=1.923 is slightly higher than that at 2.308, by approximately 2%. At $B_{r,max}$=1.923, the measured temperatures suggest higher values than at $B_{r,max}$=2.308 along the outer wall (by 1-2%) but lower at the inner wall.

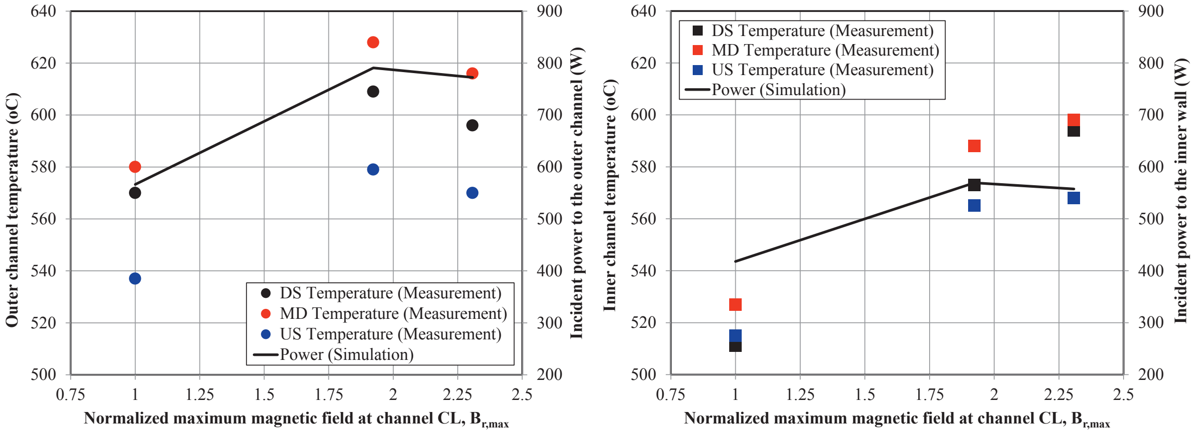

Fig 8. Temperature measurements (left axes) from thermocouples placed along the outer and inner channel of HERMeS, the locations of which are loosely identified inside the acceleration channel as downstream (DS), middle (MD) and upstream (US). Also shown is the computed incident power to the channel walls based on the Hall2De simulations (right axes). Left: Outer channel. Right: Inner channel.

It is of course recognized that power versus temperature does not constitute a one-on-one comparison. Therefore a detailed 3-D thermal model of the thruster has been developed at NASA GRC and was employed, in combination with the Hall2De results, to compare model predictions with the thermocouple measurements at the nominal operating condition of $B_{r,max}$=1. Specifically, the plasma loads from the Hall2De simulations were used as input in the thermal model and a comparison with the measurements was performed. Though it has been argued that in practice only a percentage of the incident power is absorbed by the walls [44] in these calculations the accommodation was assumed to be perfect. After a few iterations, it was found that the total power to channel walls and anode necessary to achieve agreement with the measured temperatures (1435 W) was within 1% of the value computed by Hall2De (1444 W). The comparison is shown in Fig 9-left where the filled symbol at $B_{r,max}$=1 denotes the value used by the thermal model to achieve agreement with the measurements. The thermal model results were found to be within ~20 ^{o}C of the measured values [8]. The computed power incident to the various boundaries in the Hall2De simulations is compared in Fig 9-right. The comparison shows that the anode and inner channel receive comparable power from the plasma, and range 23-39% lower than the incident power to the outer channel.

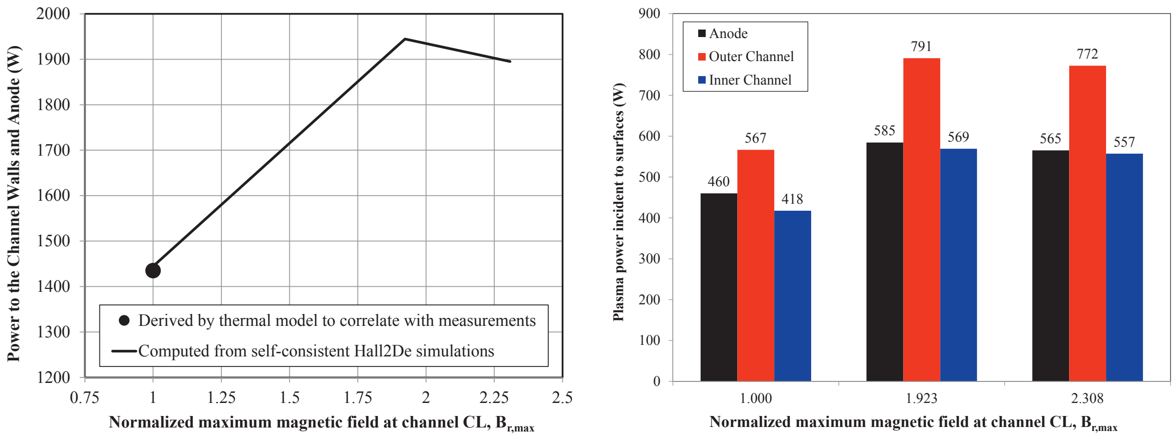

Fig 9. Left: Total incident power to the acceleration channel walls as a function of $B_{r,max}$ based on the Hall2De simulations. Also shown (by the filled symbol) is the value determined by a detailed 3-D thermal model of HERMeS, the results of which yielded close agreement (within 20 ^{o}C) with all thermocouple measurements. Right: Computed incident power to the anode, outer and inner channel walls.

The profiles of the computed incident fluxes along the walls in the channel interior (z/L≤1) are plotted in Fig 10 for electrons (left) and ions (right). As expected from the incident power results (Fig 9-left), only minor differences in the fluxes are found between $B_{r,max}$=1.923 and 2.308. The highest energy fluxes occur upstream of the acceleration zone which starts at z/L~0.8-0.9 (see also Fig 4-right), and peak within 0.4<z/L<0.8. Since the maximum fluxes occur in the ionization region it is expected that they are largely driven by the plasma density. This can indeed be seen by the electron number density contours in Fig 11. The contours show that the maximum density along the channel occurs between 0.45<z/L<0.6, which translates to slightly more downstream locations along the walls due to the curvature of the magnetic field lines. The location of the maximum fluxes is in qualitative agreement with the temperature measurements (Fig 8) which also indicate the highest values occur in the middle of the channel with the downstream locations following in magnitude. Though peak energy fluxes associated with ions are greater than those for electrons, the difference is only ~10%. A clear reduction of the fluxes is found at $B_{r,max}$=1 compared to the higher magnetic field values, which is in agreement with the temperature measurement trends in Fig 8. This reduction occurs in both electron and ion fluxes and ranges approximately 35-40%. Due to the symmetry of the magnetic field topology in the channel the energy fluxes to the outer and inner channel walls are found to be similar in magnitude. Referring to the boundaries along greyed areas in Fig 2-left, we note here that the surface area of the outer channel is 49.2% and 47.3% larger than that of the inner channel and anode, respectively. Thus, the larger power incident to the outer wall depicted in Fig 9-right is not unexpected. The larger area of the outer channel also implies that more power could be radiated away compared to the inner channel, so ultimately the thermal response of the thruster depends among others on geometrical details, contacts with other surfaces and thermal properties of the materials [8].

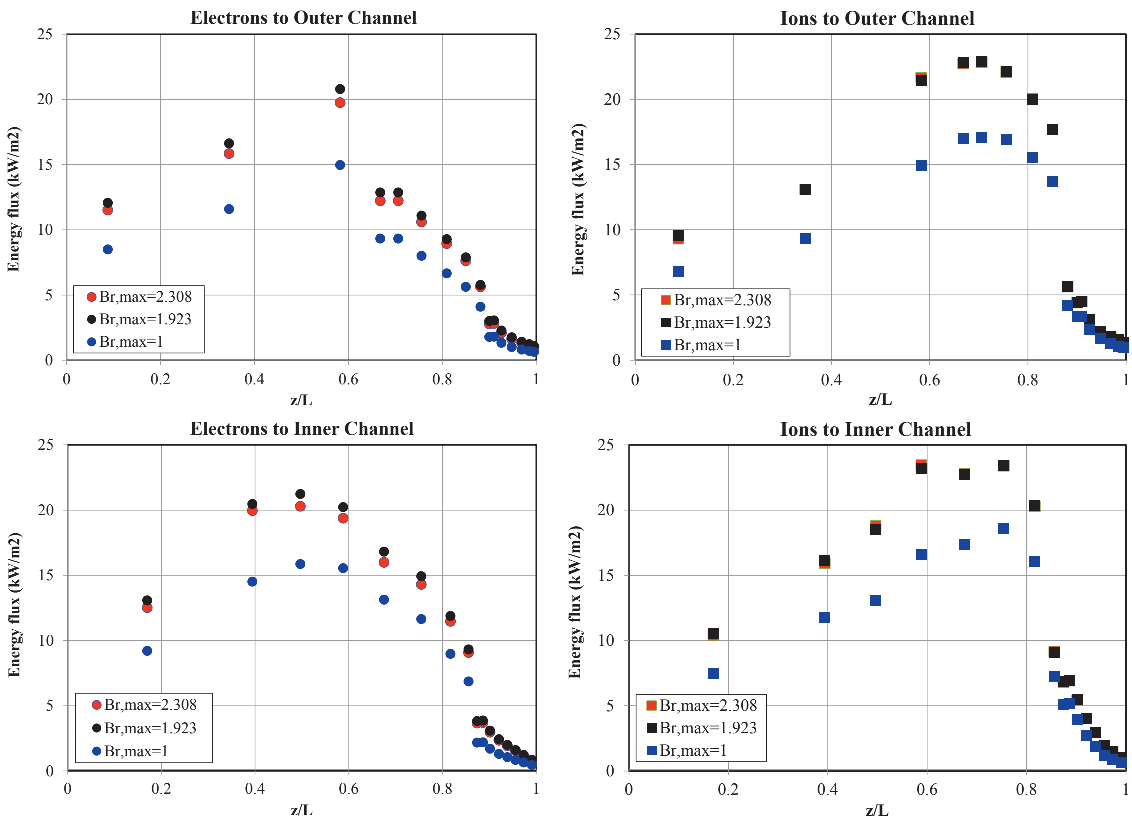

Fig 10. Computed energy fluxes to the outer (top) and inner (bottom) channel walls by electrons (left) and by ions (right) at three different values of $B_{r,max}$.

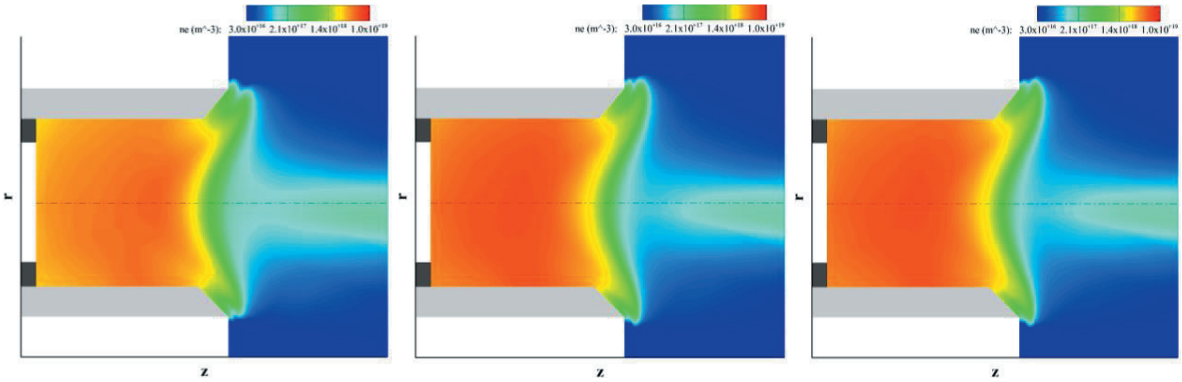

Fig 11. Contours of electron number density from the Hall2De simulations at different values of the normalized magnetic field. Left: $B_{r,max}$=1. Middle: $B_{r,max}$=1.923. Right: $B_{r,max}$=2.308.

2) Discussion

Although some of the trends related to the location of the maximum temperatures are easily explained by the simulations others are not as obvious. In this section we discuss some of the more subtle details of the results. First, we provide explanations about the reduction of the incident power at the lower magnetic fields. Because differences between the $B_{r,max}$=1.923 and 2.308 results are much smaller than those between $B_{r,max}$=1 and 2.308 we focus here only on comparison between the latter two values of $B_{r,max}$.

As it is now widely accepted, electron transport in Hall thrusters is driven largely by non-classical processes. Hall2De simulations as well as results from other codes have shown that the anomalous collision frequency needed to explain the measurements can exceed significantly the classical values. Figure 12-left plots the anomalous collision frequencies along the channel centerline in the 12.5-kW HERMeS simulations at $B_{r,max}$=1 and 2.308, and compares them with the computed classical frequencies. The variation of the anomalous frequency here has been based largely on findings from our previous work with a 6-kW laboratory Hall thruster called the H6 which shares several similar features with HERMeS. The resistive contribution to the electric field perpendicular to the magnetic field, $\mathbf{E}_\perp$, and the contribution to the work done by the electric field leading to resistive heating of the electrons are given by Eq. (7),

$$\mathbf{E}_\perp = \eta_\perp \mathbf{j}_{e\perp} \qquad \mathbf{E}_\perp \cdot \mathbf{j}_{e\perp} = \eta_\perp j_{e\perp}^{\;2} \tag{7}$$

where the perpendicular resistivity is defined here as

$$\eta_\perp = \frac{m_e \nu_e}{e^2 n_e}\left(1+\Omega_e^{\;2}\right) \sim \frac{B^2}{n_e \nu_e}\left(\Omega_e^{\;2} >> 1\right) \tag{8}$$

with j_e and Ω_e denoting the electron current density and Hall parameter, respectively. The electron mass is m_e, the charge is e and the number density is n_e. The sum of all the electron collision frequencies is given by ν_e. In the channel interior Ω_e^2 >>1and therefore it can easily be shown that the resistivity has a B^2 dependence (Eq. (8)). Hence, as the magnetic field is reduced from $B_{r,max}$=1 to 2.308 the significant decrease in the magnetic-field resistance must be followed by a reduction in ν_e to support the electric field that is required to sustain the discharge current. In the Hall2De simulations we found that the anomalous collision frequency needed to achieve the specified discharge current (Table 4) at $B_{r,max}$=1 is low enough to be comparable to or lower than the classical frequency in the channel interior. This is in contrast to the $B_{r,max}$=2.308 case in which the anomalous frequency dominates over the majority of the channel interior and exterior as shown in Fig 12-left. This finding, though beyond the scope of this paper, may have important implications on the physics of the anomalous transport and their implementation in Hall2De.

The latter is the topic of a companion paper [39]. Regarding implications on the power deposition to the walls, it is found that for z/L≳0.7, where the anomalous frequency is higher than the classical for both values of $B_{r,max}$, the reduction in the frequency (~7.7 times) is in fact greater than the reduction due to the magnetic field (~5.3 times). Thus the perpendicular resistivity in this region of the channel is in fact lower at $B_{r,max}$=2.308 than it is at 1, as plotted in Fig 12-right. As we move deeper into the channel however, the resistivity at $B_{r,max}$=2.308 exceeds that at 1 as the classical collision frequency for the second value dominates over the anomalous values. The ratio $\eta_\perp(B_{r,max}=2.308)/\eta_\perp(B_{r,max}=1)$ and the total collision frequencies are plotted in Fig 12-right.

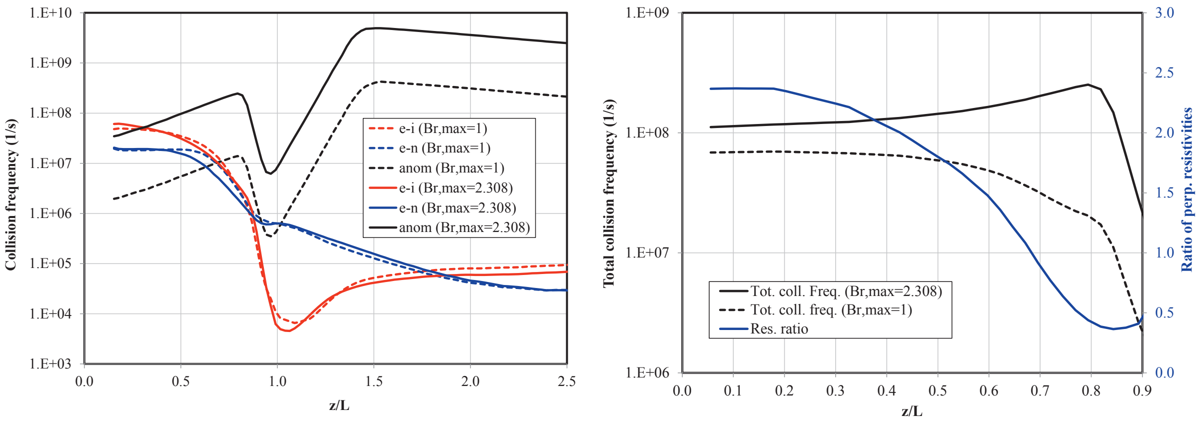

Fig 12. Left: Variation of the computed collision frequencies along the channel centerline for $B_{r,max}$ =1 and 2.308. Right: Variation of the total collision frequency (left axis) and ratio of perpendicular resistivity $\eta_\perp(B_{r,max}=2.308)/\eta_\perp(B_{r,max}=1)$ upstream of the acceleration region. (Note the channel exit is located at z/L=1)

As a consequence of the increased resistivity in the channel interior small increases in the electron temperature are observed at $B_{r,max}$=2.308 compared to $B_{r,max}$=1. The temperature variation along the channel centerline is plotted in Fig 13. Albeit small, this increase in the temperature of the electrons is found to be high enough to cause an increase in the ionization frequency. The ionization frequency for $Xe^0 \rightarrow Xe^+$ is also plotted in Fig 13-left for reference. This increased ionization then leads to higher plasma density in this region as shown in Fig 13-right. We note that the small increases in the electron temperature are still high enough to cause increased ionization at $B_{r,max}$=2.308 even though the neutral gas density is lower at this value than at $B_{r,max}$=1, as shown in Fig 13-right. The latter is a consequence of thruster operation at a lower flow rate than that at $B_{r,max}$=1 (see Table 4). This higher ionization occurs because the electron temperature in this region of the channel has diminished to low enough values (≲5 eV) for which the ionization cross section changes significantly with small changes in the temperature. This sensitivity can easily be seen in Fig 14 which plots the ionization collision frequency for $Xe^0 \rightarrow Xe^+$.

In light of the above findings we provide the following explanations of the observed trends (Sec. IIIB1) on the plasma loads as a function of the magnetic field. As $B_{r,max}$ is increased from the nominal value of 1 to higher values, the resistivity also increases in the majority of the ionization region (z/L≲0.6). This leads to small increases in the electron temperature that are high enough to increase the ionization and, in turn, the electron number density. This largely leads to the higher electron energy fluxes shown in Fig 10-left for 0.4≲z/L≲0.6. For 0.6≲z/L≲0.8, where ionization no longer drives higher densities in the high $B_{r,max}$ cases, the energy flux to the walls is dominated by ions. In this region ion acceleration has begun which also leads to the peaked profiles of the ion energy fluxes seen in Fig 10-right. The reader is also reminded here that Figs 12 and 13 are plots along the channel centerline whereas the results in Fig 10 are along the walls. Thus, due to the curvature of the magnetic field lines some displacement of the peaks is expected. This effect is well illustrated in the contours Fig 11. Regarding the slightly higher incident power computed at $B_{r,max}$=1.923 (1944.6 W) compared to that at $B_{r,max}$=2.308 (1895.0 W), we found this to be largely related to the slightly higher discharge current at which the thruster was operated when $B_{r,max}$=1.923 (see also Table 4). Specifically, we performed another Hall2De simulation at $B_{r,max}$=1.923 but in this case at 15.5 A instead of 15.57 A to duplicate the value at $B_{r,max}$=2.308. All other input parameters were the same as in the 2.308 case. We found that at $B_{r,max}$=1.923 and 15.5 A the incident power decreased to 1912.1 W and is therefore only 17.1 W higher than the value computed at $B_{r,max}$=2.308. Such differences are less than 0.9% of the total incident power and are therefore much smaller than uncertainties related to the simulations and the experiments. Other than the increase in the discharge current it is therefore not possible to identify additional mechanisms (if any) that may have caused the increase in the incident power at $B_{r,max}$=1.923 above to that at 2.308.

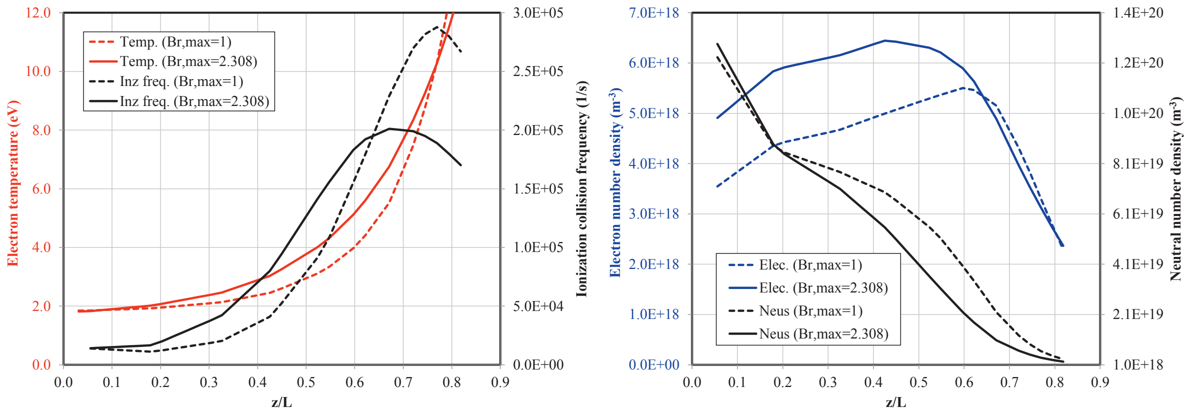

Fig 13. Computed parameters along the channel centerline in the channel interior of HERMeS, upstream of the acceleration region. Left: Electron temperature and ionization frequencies. Right: Neutral and electron number densities.

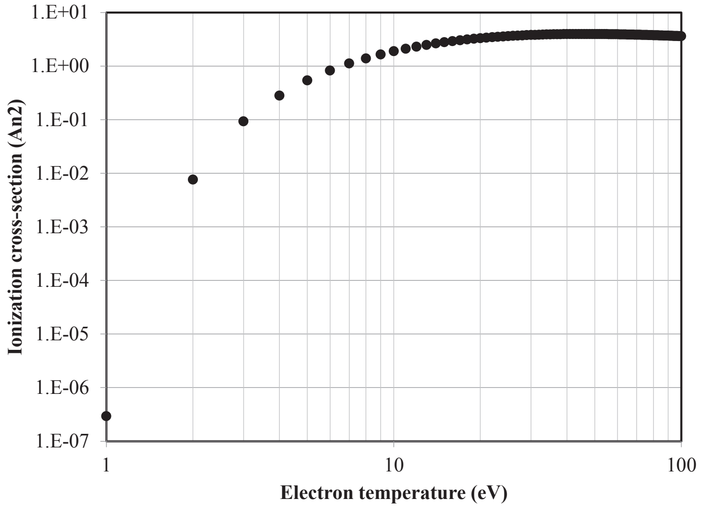

Fig 14. Variation of the cross section as function of electron temperature associated with the ionization of a xenon atom to a singly charged ion, as implemented in Hall2De (energy data based on Ref. [45]). Noted is the increasing rate of reduction as the electron temperature decreases below ~10 eV.

IV. Conclusions

The development and life qualification of HERMeS for the SEP TDM depends heavily on physics-based modeling and testing to demonstrate the performance and throughput capability of the thruster. The work presented in this paper has addressed two critical areas in the HERMeS development both directly linked to its throughput capability.

First, we have used numerical simulations with the Hall2De code to assess the effectiveness of the magnetic shielding topology in HERMeS to protect the discharge channel walls from deleterious ion bombardment. The simulation results at the conditions of highest discharge current and highest discharge voltage show that in both cases near-anode values of the plasma potential are established along these walls, and electron temperatures there are <2eV. This range of values is expected when magnetic shielding is highly effective. The results are shown to be insensitive to uncertainties in the location of the plasma and agree well with measurements provided by Langmuir probes embedded in the channel walls of the thruster. These probes yielded also near-anode potentials and electron temperatures were ≤ 5eV. The electron temperatures in HERMeS are in fact lower than those in the 6-kW H6MS which were measured to be as high as 13.3 eV. Nonetheless, in the H6MS the erosion rates were still found to be 2-3 orders of magnitude lower than those in the unshielded version of the thruster. As expected then, the simulations predict that the energy with which ions strike the walls is in most cases below the threshold for sputtering of boron nitride and thus, no measurable erosion of the HERMeS channel is expected.

Second, we have computed the electron and ion energy fluxes to determine the incident power to the channel walls. These plasma loads are used in a separate 3-D thermal model of HERMeS to assess the thruster's thermal response. The main objective of the combined plasma/thermal modeling work is to ensure that the thermal design of the thruster is robust and yields temperatures well below operating limits. In this work we have focused on the 12.5-kW, 800 operating condition which has been shown, based on the recent testing, to be the most demanding condition for the thruster in terms of thermal loads. To help, in part, determine margins for the applied magnetic field we have investigated trends associated with these plasma loads as the magnetic field is varied from the nominal condition of $B_{r,max}$=1 to the maximum value of 2.308. We found that power deposition increases by about 35% from $B_{r,max}$=1 to 2.308, largely as a result of increased ionization in the discharge chamber. This higher ionization is found to be caused by small increases in the electron temperature in the cold regions of the plasma due to increases in the electrical resistivity at the higher magnetic field strengths. At the 12.5-kW 800-V condition, the fluxes to the walls are found to peak towards the middle and downstream locations of the channel walls. This is in general agreement with thermocouple measurements obtained during recent testing of the thruster that yielded higher temperatures along these regions of the walls.

Acknowledgments

The support of the joint NASA GRC and JPL development of HERMeS by NASA's Space Technology Mission Directorate through the Solar Electric Propulsion Technology Demonstration Mission (SEP TDM) project is gratefully acknowledged. The authors also wish to acknowledge Rohit Shastry for providing the wall probe measurements along the HERMeS acceleration channel. Portions of the research described in this paper were carried out at the Jet Propulsion Laboratory, California Institute of Technology, under a contract with the National Aeronautics and Space Administration.

References

[1] J. R. Brophy, R. Gershman, D. Landau, J. Polk, C. Porter, D. Yeomans, C. Allen, W. Williams, and E. Asphaug, "Asteroid Return Mission Feasibility Study," presented at the 47th AIAA/ASME/SAE/ASEE Joint Propulsion Conference, San Diego, CA, AIAA-2011-5565, July 2011.

[2] J. R. Brophy and S. Oleson, "Spacecraft Conceptual Design for Returning Entire near-Earth Asteroids," presented at the 48th AIAA/ASME/SAE/ASEE Joint Propulsion Conference, Atlanta, GA, AIAA-2012-4067, July 2012.

[3] I. G. Mikellides, I. Katz, R. R. Hofer, D. M. Goebel, K. de Grys, and A. Mathers, "Magnetic shielding of the channel walls in a Hall plasma accelerator," *Physics of Plasmas,* vol. 18, p. 033501, Mar 2011.
[4] I. G. Mikellides, I. Katz, R. R. Hofer, and D. M. Goebel, "Magnetic shielding of walls from the unmagnetized ion beam in a Hall thruster," *Applied Physics Letters,* vol. 102, Jan 14 2013.
[5] R. R. Hofer, D. Herman, J. E. Polk, H. Kamhawi, and I. G. Mikellides, "Development Approach and Status of the 12.5 kW HERMeS Hall Thruster for the Solar Electric Propulsion Technology Demonstration Mission " presented at the 34th International Electric Propulsion Conference, Hyogo-Kobe, Japan, IEPC-2015-186, July 2015.
[6] D. A. Herman, J. E. Polk, R. R. Hofer, W. Santiago, H. Kamhawi, R. Scheidegger, and L. Pinero, "The Development of the Ion Propulsion System for the Solar Electric Propulsion Technology Demonstration Mission " presented at the 34th International Electric Propulsion Conference, Hyogo-Kobe, Japan, IEPC-2015-008, July 2015.
[7] H. Kamhawi, T. Haag, W. Huang, D. A. Herman, R. Thomas, R. Shasrty, J. Yim, L. Chang, L. Clayman, T. Verhey, C. Griffith, J. Myers, G. Williams, I. G. Mikellides, R. R. Hofer, J. E. Polk, and B. A. Jorns, "Performance Characterization of the Solar Electric Propulsion Technology Demonstration Mission 12.5-kW Hall Thruster," presented at the 34th International Electric Propulsion Conference, Hyogo-Kobe, Japan, IEPC-2015-007, July 2015.
[8] J. Myers, H. Kamhawi, and J. Yim, "HERMeSThermal Model," presented at the 34th International Electric Propulsion Conference, Hyogo-Kobe, Japan, IEPC-2015-XXX, July 2015.
[9] I. G. Mikellides, I. Katz, R. R. Hofer, and D. M. Goebel, "Magnetic shielding of a laboratory Hall thruster. I. Theory and validation," *Journal of Applied Physics,* vol. 115, Jan 28 2014.
[10] R. R. Hofer, D. M. Goebel, I. G. Mikellides, and I. Katz, "Magnetic shielding of a laboratory Hall thruster. II. Experiments," *Journal of Applied Physics,* vol. 115, Jan 28 2014.
[11] I. G. Mikellides and I. Katz, "Numerical simulations of Hall-effect plasma accelerators on a magnetic-field-aligned mesh," *Physical Review E,* vol. 86, p. 046703, Oct 17 2012.
[12] J. M. Haas, R. R. Hofer, D. L. Brown, B. M. Reid, and A. D. Gallimore, presented at the 54th JANNAF Propulsion Meeting, Denver, CO, 2007.
[13] H. Kamhawi, T. W. Haag, D. T. Jacobson, and D. H. Manzella, "Performance Evaluation of the NASA-300M 20 kW Hall Effect Thruster," presented at the 47th AIAA/ASME/SAE/ASEE Joint Propulsion Conference, San Diego, CA, AIAA-2011-5521, July 2011.
[14] I. G. Mikellides, I. Katz, H. Kamhawi, and J. L. Vannoord, "Numerical Simulations of a 20-kW Class Hall Thruster Using the Magnetic-Field-Aligned-Mesh Code Hall2De," presented at the 32nd International Electric Propulsion Conference, Wiesbaden, Germany, IEPC-2011-244, September 2011.
[15] H. Kamhawi, W. Huang, T. Haag, R. Shastry, G. Soulas, T. Smith, I. G. Mikellides, and R. R. Hofer, "Performance and Thermal Characterization Tests of the NASA-300MS 20 kW Hall Effect Thruster," presented at the 33rd International Electric Propulsion Conference, Washington, DC, IEPC-2013-444, October 2013.
[16] I. G. Mikellides, R. R. Hofer, I. Katz, and D. M. Goebel, "The Effectiveness of Magnetic Shielding in High-Isp Hall Thrusters," presented at the 49th AIAA/ASME/SAE/ASEE Joint Propulsion Conference, San Jose, CA, AIAA-2013-3885, July 2013.
[17] R. R. Hofer, B. A. Jorns, J. E. Polk, I. G. Mikellides, and J. S. Snyder, "Wear Test of a Magnetically Shielded Hall Thruster at 3000 Seconds Specific Impulse," presented at the 33rd International Electric Propulsion Conference, Washington, DC, IEPC-2013-033, October 2013.
[18] I. G. Mikellides, R. R. Hofer, I. Katz, and D. M. Goebel, "Magnetic shielding of Hall thrusters at high discharge voltages," *Journal of Applied Physics,* vol. 116, Aug 7 2014.
[19] I. Katz and I. G. Mikellides, "Neutral gas free molecular flow algorithm including ionization and walls for use in plasma simulations," *Journal of Computational Physics,* vol. 230, pp. 1454-1464, Feb 20 2011.

[20] I. G. Mikellides, I. Katz, and R. R. Hofer, "Design of a Laboratory Hall Thruster with Magnetically Shielded Channel Walls, Phase I: Numerical Simulations," presented at the 47th AIAA/ASME/SAE/ASEE Joint Propulsion Conference, San Diego, CA, AIAA-2011-5809, July 2011.
[21] I. G. Mikellides, I. Katz, R. R. Hofer, and D. M. Goebel, "Design of a Laboratory Hall Thruster with Magnetically Shielded Channel Walls, Phase III: Comparison of Theory with Experiment," presented at the 48th AIAA/ASME/SAE/ASEE Joint Propulsion Conference, Atlanta, GA, AIAA-2012-3789, July 2012.
[22] N. B. Meezan, W. A. Hargus, and M. A. Cappelli, "Anomalous electron mobility in a coaxial Hall discharge plasma," *Physical Review E,* vol. 63, p. 026410, Feb 2001.
[23] A. Ducrocq, J. C. Adam, A. Heron, and G. Laval, "High-frequency electron drift instability in the cross-field configuration of Hall thrusters," *Physics of Plasmas,* vol. 13, Oct 2006.
[24] A. Lazurenko, T. D. de Wit, C. Cavoit, V. Krasnoselskikh, A. Bouchoule, and M. Dudeck, "Determination of the electron anomalous mobility through measurements of turbulent magnetic field in Hall thrusters," *Physics of Plasmas,* vol. 14, Mar 2007.
[25] C. Boniface, L. Garrigues, G. J. M. Hagelaar, J. P. Boeuf, D. Gawron, and S. Mazouffre, "Anomalous cross field electron transport in a Hall effect thruster," *Applied Physics Letters,* vol. 89, Oct 16 2006.
[26] J. C. Adam, A. Heron, and G. Laval, "Study of stationary plasma thrusters using two-dimensional fully kinetic simulations," *Physics of Plasmas,* vol. 11, pp. 295-305, Jan 2004.
[27] P. Coche and L. Garrigues, "A two-dimensional (azimuthal-axial) particle-in-cell model of a Hall thruster," *Physics of Plasmas,* vol. 21, Feb 2014.
[28] A. Harten, P. D. Lax, and B. Vanleer, "On Upstream Differencing and Godunov-Type Schemes for Hyperbolic Conservation-Laws," *Siam Review,* vol. 25, pp. 35-61, 1983.
[29] A. Lopez Ortega and I. G. Mikellides, "A New Cell-Centered Implicit Numerical Scheme for Ions in the 2-D Axisymmetric Code Hall2De," presented at the 50th AIAA/ASME/SAE/ASEE Joint Propulsion Conference, Cleveland, OH, AIAA-2014-3621, July 2014.
[30] J. C. Butcher, "Numerical methods for ordinary differential equations in the 20th century," *Journal of Computational and Applied Mathematics,* vol. 125, pp. 1-29, Dec 15 2000.
[31] R. Sullivan, "The Physics of High-Velocity Ions in the Hall Thruster Near-Field," Ph.D., California Institute of Technology, 2010.
[32] I. G. Mikellides, A. L. Ortega, and B. A. Jorns, "Assessment of Pole Erosion in a Magnetically Shielded Hall Thruster," presented at the 50th AIAA/ASME/SAE/ASEE Joint Propulsion Conference, Cleveland, OH, AIAA-2014-3897, July 2014.
[33] A. Lopez Ortega, I. G. Mikellides, and I. Katz, "Hall2De Numerical Simulations for the Assessment of Pole Erosion in a Magnetically Shielded Hall Thruster," presented at the 34th International Electric Propulsion Conference, Hyogo-Kobe, Japan, IEPC-2015-249, July 2015.
[34] G. D. Hobbs and J. A. Wesson, "Heat Flow through a Langmuir Sheath in Presence of Electron Emission," *Plasma Physics,* vol. 9, pp. 85-87, 1967.
[35] J. M. Fife, "Hybrid-PIC modeling and electrostatic probe survey of Hall thrusters," Ph.D., Massachusetts Institute of Technology, 1998.
[36] J. Bareilles, G. J. M. Hagelaar, L. Garrigues, C. Boniface, J. P. Boeuf, and N. Gascon, "Critical assessment of a two-dimensional hybrid Hall thruster model: Comparisons with experiments," *Physics of Plasmas,* vol. 11, pp. 3035-3046, 2004.
[37] C. A. Thomas and M. A. Cappelli, "Anomalous electron transport in the Hall-effect thruster," Ph.D., Stanford University, 2006.
[38] W. A. Hargus and M. A. Cappelli, "Investigation of the plasma acceleration mechanism within a coaxial Hall thruster," Ph.D., Stanford University, 2001.
[39] I. Katz , I. G. Mikellides, B. A. Jorns, and A. Lopez Ortega "Hall2De Simulations with an Anomalous Transport Model Based on the Electron Cyclotron Drift Instability," presented at the

34th International Electric Propulsion Conference, Hyogo-Kobe, Japan, IEPC-2015-402, July 2015.

[40] R. Shastry, W. Huang, T. W. Haag, and H. Kamhawi, "Langmuir Probe Measurements within the Discharge Channel of the 20-kW NASA-300M and NASA-300MS Hall," presented at the 33rd International Electric Propulsion Conference, Washington, DC, IEPC-2013-122, October 2013.

[41] R. Shastry. (2011). *Experimental Characterization of the Near-Wall Region in Hall Thrusters and its Implications on Performance and Lifetime*. Available: http://hdl.handle.net/2027.42/84654

[42] R. Shastry, W. Huang, and H. Kamhawi, "Near-Surface Plasma Characterization of the 12.5-kW NASA TDU1 Hall Thruster," presented at the 51st AIAA/SAE/ASEE Joint Propulsion Conference, Orlando, FL, AIAA-2015-XXXX, July 2015.

[43] I. G. Mikellides, I. Katz, D. M. Goebel, and J. E. Polk, "Hollow cathode theory and experiment. II. A two-dimensional theoretical model of the emitter region," *Journal of Applied Physics,* vol. 98, Dec 1 2005.

[44] V. Kim, A. Semenov, and I. Shkarban, "Investigation of the Accelerated Ions Energy Accommodation Under Their Impingement With Solid Surfaces," presented at the 38th AIAA/ASME/SAE/ASEE Joint Propulsion Conference, Indianapolis, IN, AIAA-2002-4110, July 2002.

[45] R. Rejoub, B. G. Lindsay, and R. F. Stebbings, "Determination of the absolute partial and total cross sections for electron-impact ionization of the rare gases," *Physical Review A,* vol. 65, Apr 2002.